

RESEARCH ARTICLE

Numerical Analysis of Aerodynamic and Shock Wave Characteristics of Biconvex and Double-Wedge Shape Airfoils for Supersonic Flow

Md. Zulkarna-En¹, Md. Ashraful Islam^{1*}, Abdullah Al-Faruk¹, Md Rhyhanul Islam Pranto¹ and A.N.M. Mominul Islam Mukut^{2*}

¹Department of Mechanical Engineering, Khulna University of Engineering & Technology, Khulna-9203, Bangladesh

²Department of Mechanical Engineering, Dhaka University of Engineering and Technology, Gazipur-1707, Bangladesh

ABSTRACT - This present study describes the aerodynamic characteristics of supersonic flow over biconvex and double wedge airfoils using a finite volume method-based commercial CFD code Ansys Fluent. A steady-state RANS approach is used with SST k- ω viscous modeling. A series of simulations are conducted to analyze the characteristics of shock and expansion waves formed around the airfoils for Mach numbers ranging from 1.4 to 3.4 with varying angles of attack (α) from 0° to 20°. It is observed that the lift and drag coefficients both increase with the angle of attack for a fixed Mach number and decrease with the Mach number for a fixed angle of attack. Double wedge airfoil generates about 5% more lift at a low Mach number and 1% more lift at a higher Mach number compared to the biconvex airfoil. However, the biconvex airfoil generates lesser drag than the double wedge airfoil. The maximum value of the pressure coefficient (C_p) is found to be 1.7 for biconvex airfoil and 1.4 for double wedge airfoil. The maximum value of the lift-to-drag ratio for biconvex airfoil is 7.63, occurs at 1.4 Mach number and 3.46° angle of attack, whereas the value for double wedge airfoil is 5.19 at the same Mach number with 4.47° angle of attack, which suggest that biconvex airfoil has a higher lift-to-drag ratio and gives a better aerodynamics performance. The shock waves start to detach after an angle of attack of 5° and the shock wave is fully detached at a 15° angle of attack for biconvex airfoil for Mach number of 1.4. For the same Mach number, the double wedge airfoil, the shock wave starts to form the same as the biconvex airfoil but the waves are fully detached at a lower angle of attack of 10°. With the increasing Mach number, the shock waves remain attached to the airfoil.

ARTICLE HISTORY

Received : 06th April 2023
 Revised : 19th Sep. 2023
 Accepted : 25th Oct. 2023
 Published : 26th Dec. 2023

KEYWORDS

Airfoil
Mach number
Shock wave
Supersonic
CFD

1.0 INTRODUCTION

Supersonic flow over aerospace structures has a wide variety of applications in aeronautics. In the field of aerospace engineering, biconvex and double-wedge airfoils are utilized frequently, and the experts have produced a great deal of work in this area. Both biconvex and double-wedge airfoils are utilized by supersonic aircraft; however, analysis data for any of these two airfoils is not easily accessible [1]. The existence of these entities within the flow field of supersonic flows gives rise to singularities in the flow, including shock and expansion waves. The presence of these singularities in the context of utilizing such airfoils during supersonic flight leads to an augmentation of the unfavorable drag. The presence of wave drags and shape, and skin-friction drag is commonly acknowledged in the field. It has been shown that minimizing this particular aspect of drag is achievable by maintaining the attachment of the shock to the body during flight. The reduction in drag can be accomplished through the implementation of a thinner cross-section, as well as the incorporation of sharp leading and trailing edges. This is in contrast to subsonic airfoils, which possess rounded leading edges that result in a detached shock, resulting in increased drag as compared to airfoils with attached shocks[2-4]. It is important to know the aerodynamic parameters to design such wings.

A symmetrical biconvex airfoil with a slightly curved leading edge and 6% thickness was studied by Bensiger and Prasanth [5]. They used Gambit software to design and mesh the airfoil and ANSYS Fluent software to simulate and show the aerodynamic characteristics of the biconvex airfoil. They concluded that this airfoil could also be used in hypersonic vehicles. Hamid et al. [6] investigated the properties of compressible flow around a biconvex arc airfoil that was placed in a channel. They did numerical computation for a 12% thick biconvex circular arc airfoil in a two-dimensional medium. For the purpose of the numerical investigation, they utilized Reynolds-averaged Navier-Stokes equations in conjunction with shear stress transfer (SST) turbulence models. They discovered that an uneven shock motion generates a temporary interaction between the shock and the boundary layer, leading to an erratic separation. Because of unstable shock oscillation, both the Mach number of shocks and the locations of shock waves exhibit a periodic pattern of behavior. This unstable separation brings about the self-excited shock oscillation. Kinaci [7] investigated supersonic flow over a double circular airfoil with varying radius. He created the airfoil in Gridgen V15, a mesh generation program, and simulated it in Star-CCM+. He demonstrated the location and magnitude of leading and trailing edge shocks. He also computed the lift and drag coefficients. A few studies investigated supersonic natural laminar flow on a biconvex airfoil wing [8, 9]. They studied the behavior of a thin airfoil at supersonic speeds using supersonic natural laminar flow, and the thin airfoil was used to design wings for a Supersonic Business Jet (SBJ). They concluded that, as a result of the iterative nature of

flow simulation, the lift and drag coefficients and forces based on analytical and numerical calculations are nearly identical and satisfactory. They also calculated the highest pressure and temperature analytically and numerically [1]. Tulia et al. [10] analyzed periodic transonic flow over 14% and 18% thick biconvex airfoils. They have investigated the flow control technique and surface cooling concept as a contour bump separately. They have emphasized the flow control technique to reduce drag at transonic Mach number. However, they did not mention what would happen in the supersonic region or whether the flow control technique could be applicable in the supersonic region or not. D. H. Williams et al. [11] experimented on a 5% thick biconvex airfoil in a Compressed Air Tunnel and analyzed the aerodynamic coefficient C_L and C_D at subsonic region. But at supersonic speed, the values of lift coefficient, C_L and drag coefficient, C_D may vary as there will be shock waves. W. P. Jones and Sylvia W. Skan [12] developed a technique for calculating the aerodynamic coefficients for an oscillating airfoil. For different frequencies, aerodynamic lift and pitching moment derivatives are given for a 5% thick, symmetrical, circular-arc airfoil at Mach numbers of 1.4, 1.5, and 2.0 and compared to values obtained based on the flat plate theory. At the lower Mach numbers, the effect of thickness seems to be important, and the results indicate that the flat plate theory is not sufficiently precise.

Robert J. McGhee et al. [13] conducted an experiment to determine the low-speed two-dimensional aerodynamic characteristics of a 13% thick airfoil designed for general aviation applications in the Langley low-turbulence pressure tunnel. They showed that maximum section lift coefficients climbed fast at Reynolds numbers between 2×10^6 and 6×10^6 and reached values larger than 2.0 for the plain airfoil and greater than 3.0 with a 20% chord-split flap deflected 60 degrees, according to the investigation's findings. Olejniczak et al. [14] analyzed a double-wedge airfoil numerically and experimentally, measured the surface pressure heat-transfer rate, and visualized the flow using interferometry. They demonstrated that computed separation zones are smaller than those seen in the experimental investigation. They found that CFD's failure to match experiments in calculating the separation areas is not due to grid resolution effects, viscous conditions modeling, turbulence, or flow unsteadiness but the inadequate models of real gas and vibrational unbalancing effects. Solomon and Hennery [12] investigated aerodynamic coefficients of 4% and 6% thickness ratios for two symmetrical double-wedge airfoils and compared them with the NACA 65-206 airfoils. At subsonic speeds, the double-wedge airfoil exhibited no distinguishable features other than those of usual subsonic profiles like that of NACA 65-series airfoils of small thickness ratios. However, unlike the subsonic profile, the lift curve slope varied with the Mach number. At low Mach numbers, the maximum lift coefficients of the double-wedge airfoil were comparable to the 6% thickness ratio of symmetric NACA airfoils. They showed that the drag coefficient of the double-wedge airfoil was lower than that of conventional airfoils at low speeds but at high speeds. Furthermore, a number of recent investigations have been carried out for high-speed aerodynamics [15-18]. The aerodynamic characteristics of biconvex and double wedge airfoils can be analyzed in many ways; however, they are mainly classified into two types: (a) high-fidelity and (b) low-fidelity techniques. The first one includes experimental measurements and numerical simulations, and the second includes shock expansion and linearized theories [19]. The CFD method can be very helpful to analyze and obtain the results of the aerodynamic characteristics of a supersonic airfoil.

In the present work, an attempt is made to analyze the aerodynamic characteristics at high Mach numbers and compressible flow of 2D biconvex and double wedge airfoils with varying angles of attack. The work also includes analyzing different shock waves and their effect on the airfoils. Finally, a comparison of numerical results between these two airfoils will be studied. The numerical simulations are carried out using ANSYS Fluent, and comparisons are made to determine which airfoil performs better at supersonic speed.

2.0 METHOD

In this present study, biconvex and Double-wedge supersonic airfoils are chosen. The geometry of the selected airfoils is created using SpaceClaim. The design of the airfoils is in a two-dimensional shape and a chord length of 1 meter. The Computational Fluid Dynamics (CFD) approach was used within the ANSYS program to carry out a number of simulations, and the results were analyzed. The CFD package mainly works as a Pre-processor, solver, and post-processor. In pre-processor geometry and meshing are included. The solver solves the problem numerically using boundary conditions and various turbulence modeling in the solver. In the post-processor, the analysis of the results is done. In ANSYS, a Fluent RANS-based solver was used, and an SST k- ω viscous model was used for viscous modeling.

2.1 Airfoil

For simulation in this work, two different types of airfoils are chosen: (I) a double-wedge airfoil and (II) a biconvex airfoil. Both of these are examples of supersonic airfoils. Typically, supersonic airfoils have a narrow section that is composed of angled planes or opposing arcs (these types of airfoils are referred to as "Double-Wedge airfoils" and "biconvex airfoils," respectively). These airfoils often have very low thickness-to-chord ratios; hence, it is important to note that they are relatively thin. The sharp edges of the airfoil ensure that there is no development of a separate bow shock in front of the airfoil as it travels through the air [20].

In contrast, subsonic airfoils usually have rounded leading edges to reduce flow separation over a wide range of angles of attack. This helps the airfoil perform better at lower speeds [21]. When traveling at supersonic speeds, a rounded edge will behave just like a blunt body, which will cause a bow shock and significantly increase the amount of wave drag. Modifications are made to the thickness, camber, and angle of attack of the airfoils in order to get a design that results in

a slight deviation from the path taken by the airflow in the surrounding environment [22]. The simulation unit cord length of 1 meter is selected for both airfoils. ANSYS SpaceClaim created airfoil geometry. As the flow past these airfoils is supersonic, there are shock waves, namely oblique shock and expansion shock waves. The oblique shock is created at both airfoils' leading and trailing edges. An expansion wave region is observed whenever the flow is turned away from the surface, as shown in Figure 2.

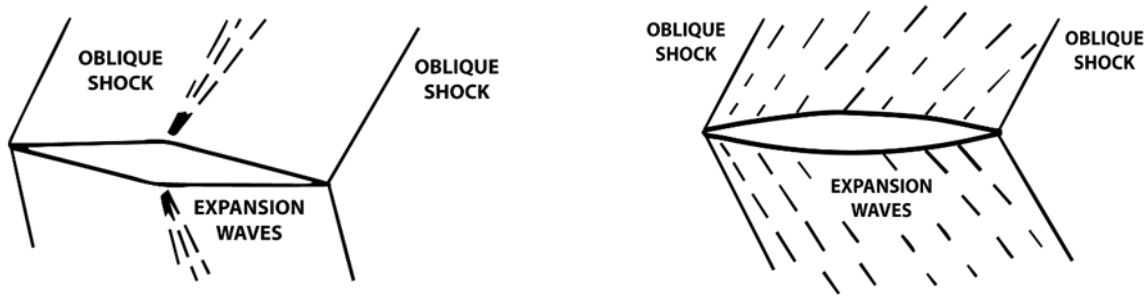


Figure 1. Supersonic flow over Double-Wedge airfoil (left) and biconvex airfoil (right)

2.2 Airfoil Geometry

The geometry of the Double-wedge airfoil is generated using SpaceClaim (Shown in Figure 1). Where M_∞ represents the Free Stream Mach Number, α is the Angle of Attack, C is the chord length, set equal to 1 meter, δ is the half wedge angle, set equal to 5° , and t represents the maximum thickness. The top and bottom surfaces of the biconvex airfoil are generated using two sets of equations, $\frac{y_u}{C} = 0.1 \frac{x}{C} (1 - \frac{x}{C})$ and $\frac{y_l}{C} = -0.1 \frac{x}{C} (1 - \frac{x}{C})$, respectively, Where C is 1 meter, which gives a unit chord 5% thick biconvex airfoil, as shown in Figure 3.

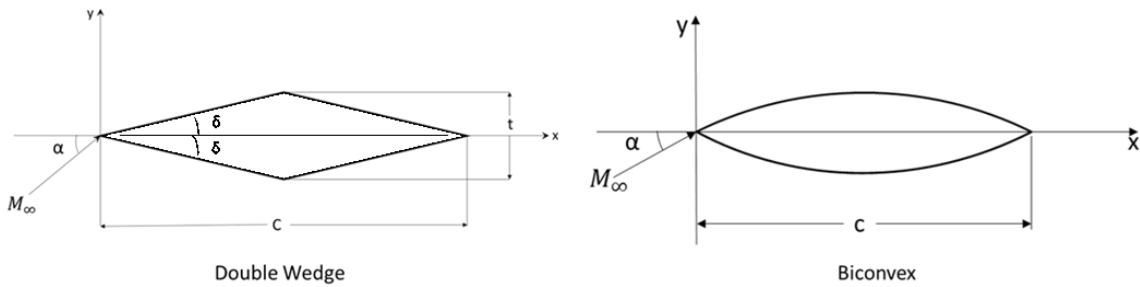


Figure 1. Airfoil Geometry

2.3 Governing Equations

Flow past the airfoil is 2D and in supersonic range or Mach number, $M > 1$, so the flow is compressible. So, compressible Continuity, Navier-Stokes, and Energy equations are chosen for Governing Equations for the flow field [23]. So, the governing equations of steady and 2D compressible flow can be expressed as:

$$\frac{\partial(\rho u)}{\partial x} + \frac{\partial(\rho v)}{\partial y} = 0 \tag{1}$$

$$u \frac{\partial(\rho u)}{\partial x} + v \frac{\partial(\rho u)}{\partial y} = -\frac{\partial P}{\partial x} + \frac{\partial \tau_{xx}}{\partial x} + \frac{\partial \tau_{yx}}{\partial y} \tag{2}$$

$$u \frac{\partial(\rho v)}{\partial x} + v \frac{\partial(\rho v)}{\partial y} = -\frac{\partial P}{\partial y} + \frac{\partial \tau_{xy}}{\partial x} + \frac{\partial \tau_{yy}}{\partial y} \tag{3}$$

$$\rho c_v \frac{dT}{dt} = k \nabla^2 T + \phi \tag{4}$$

here,

$$\tau_{xx} = 2\mu \frac{\partial u}{\partial x}$$

$$\tau_{yy} = 2\mu \frac{\partial v}{\partial y}$$

$$\tau_{xy} = \tau_{yx} = \mu \left(\frac{\partial u}{\partial y} + \frac{\partial v}{\partial x} \right)$$

$$\phi = \mu \left[2 \left(\frac{\partial u}{\partial x} \right)^2 + 2 \left(\frac{\partial v}{\partial y} \right)^2 + \left(\frac{\partial u}{\partial y} + \frac{\partial v}{\partial x} \right)^2 \right]$$

Where, equation (1) is the continuity, equations (2) and (3) are the Navier-Stokes, and equation (4) is the energy equation. u and v are the velocity in the x and y direction, respectively, μ is the viscosity, ρ is density, p is pressure, τ is shear stress, ϕ is viscous dissipation function, and T is temperature.

2.4 Computational Method

The present study used ANSYS Fluent software to run the simulations. The simulations were performed for a variety of different Mach numbers 1.4 to 4.4, varying the angle of attack. As the flow is compressible i.e., density is not constant, so density-based solver was selected. The energy equation was turned on. The fluid flow over the airfoil is also turbulent, so the RANS equation was solved. The RANS is a time-averaged equation and can be expressed as:

$$\frac{\partial(\rho u_i)}{\partial x_i} = 0 \quad (5)$$

$$\frac{\partial(\rho u_i u_j)}{\partial x_j} = \frac{\partial p}{\partial x_i} + \frac{\partial}{\partial x_j} \left[\mu \left(\frac{\partial u_i}{\partial x_j} + \frac{\partial u_j}{\partial x_i} - \frac{2}{3} \delta_{ij} \frac{\partial u_l}{\partial x_l} \right) \right] + \frac{\partial}{\partial x_j} (-\rho \overline{u'_i u'_j}) \quad (6)$$

here,

u = velocity of the fluid

ρ = density of the fluid

μ = dynamic viscosity of the fluid

On the left-hand side of this equation is the definition of the fluid element's mean momentum change due to flow instability and convection caused by the mean flow. The Reynolds stress $(-\rho \overline{u'_i u'_j})$ regulates this adjustment, which is governed by the mean body force, isotropic stress due to the mean pressure field, viscous stresses, and visible stress due to the fluctuating velocity field. To solve the RANS equations, this nonlinear stress term necessitates additional modeling, which has resulted in a wide range of turbulence models [24-26].

In the present work for turbulence modeling SST (Shear Stress Transport), the $k-\omega$ turbulence model is used to capture the turbulence effect for the flow over the airfoil and is described in the next section.

2.5 SST $k-\omega$ Model

Shear Stress Transport (SST) $k-\omega$ is a popular eddy-viscosity turbulence mode that is modeled with two equations in CFD analysis. Menter developed the shear-stress transport (SST) $k-\omega$ model to combine the $k-\omega$ model's robust and accurate formulation in the near-wall region with the $k-\epsilon$ model's free-stream independence in the far field. The $k-\epsilon$ model is converted to a $k-\omega$ formula to accomplish this. The SST $k-\omega$ model is similar to the standard $k-\omega$ model, with the following improvements [27-29]:

- i. The $k-\omega$ standard model and the transformed $k-\epsilon$ are combined and added with a mixing function. The blending function is designed to be one in the neighborhood where the standard $k-\omega$ model is activated, the surface is zero away, and the transformed $k-\epsilon$ model is activated.
- ii. The SST model contains in the omega equation a damp cross-cutting term.
- iii. In addition, the turbulent shear stress is expressed, and the description of the turbulent viscosities is improved.
- iv. There are different modeling constants.

The turbulent kinetic energy, k , and the eddy viscosity dissipation rate, ω are determined by using the following transport equations:

$$\frac{\partial(\rho k)}{\partial t} + \frac{\partial(\rho k u_i)}{\partial x_i} = \frac{\partial}{\partial x_j} \left(\Gamma_k \frac{\partial k}{\partial x_j} \right) + G_k - Y_k + S_k \quad (7)$$

$$\frac{\partial(\omega k)}{\partial t} + \frac{\partial(\rho \omega u_i)}{\partial x_i} = \frac{\partial}{\partial x_j} \left(\Gamma_\omega \frac{\partial \omega}{\partial x_j} \right) + G_\omega - Y_\omega + D_\omega + S_\omega \quad (8)$$

G_k denotes the generation of turbulence kinetic energy due to mean velocity gradients in these two equations. G_ω stands for the generation of ω . The effective diffusivity of k and ω , respectively, is represented by Γ_k and Γ_ω , which can be calculated as described below. The dissipation of k and ω due to turbulence is represented by

Y_k and Y_ω . D_ω represents the cross-diffusion term, calculated as described below. S_k and S_ω are user-defined source terms.

The effective diffusivities for the SST $k-\omega$ model are given by,

$$\Gamma_k = \mu + \frac{\mu_t}{\sigma_k}$$

$$\Gamma_\omega = \mu + \frac{\mu_t}{\sigma_\omega}$$

Where, σ_k and σ_ω represents the turbulent Prandtl numbers for k and ω , respectively and μ_t represents turbulent viscosity and can be calculated by the following expression,

$$\mu_t = \frac{\rho k}{\omega} \frac{1}{\max\left[\frac{1}{\alpha^* a_1 \omega}, SF_2\right]}$$

where S is the strain rate magnitude, α is the angle of attack and $\sigma_k = \frac{1}{\sigma_{k,1} + \frac{(1-F_1)}{\sigma_{k,2}}}$, $\sigma_\omega = \frac{1}{\sigma_{\omega,1} + \frac{(1-F_1)}{\sigma_{\omega,2}}}$ and F_1, F_2 are the blending functions.

2.6 Computational Domain and Boundary Conditions

A computation C-type domain is created to run the simulations around the Double-Wedge and biconvex airfoils. A chord length (C) of 1 m is selected for both airfoils. The domain is extended by $12.5C$ upstream and $20C$ downstream from the trailing edge to minimize the boundary effect [30], as shown in Figure 3. For simulation, the airfoil surface is selected as a no-slip boundary condition. The outer domain ABCDEF is selected as a pressure-farfield boundary condition where the velocity is inputted as Mach number (M). Instead of rotating the airfoils, the angle of attack (α) was changed in the present simulations by changing the direction of flow, which had the same effect on the airfoils. The x and y components of the flow can be calculated by $M\cos(\alpha)$ and $M\sin(\alpha)$, respectively, for different angle of attack (α).

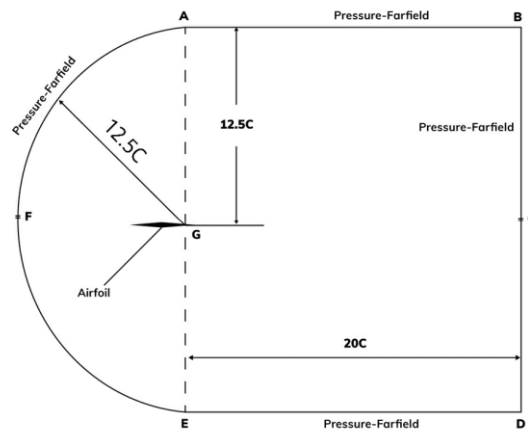


Figure 2. Computational domain and boundary conditions

2.7 Meshing

The meshing of the computational domain containing the Biconvex and Double-Wedge airfoils was completed by the commercial software ANSYS Meshing. The C-type structural mesh was developed to improve the wall function and for better convergence. The meshing with quadrilateral elements for the whole domain surrounding the Double-Wedge and biconvex airfoils is shown in Figure 4. By dividing circular and rectangular sections of the domain with different edge sizing, a different number of meshes were developed. Around the airfoils, a denser mesh was generated to capture the viscous and shock wave effect over the surface of the airfoils. The application of the wall function near the airfoil significantly controls the solution and processing time. The non-dimensional wall parameter is defined as:

$$y^+ = y \times \frac{\sqrt{(\tau\omega/\rho)}}{\mu} \tag{9}$$

Here y is the distance of the wall to the centroid of the first cell. It is also known as the first cell height. The y^+ is maintained around 0.23 for the biconvex and 0.27 for the double wedge airfoil. Biasing was done near the airfoil region to control the nearby wall y^+ value.

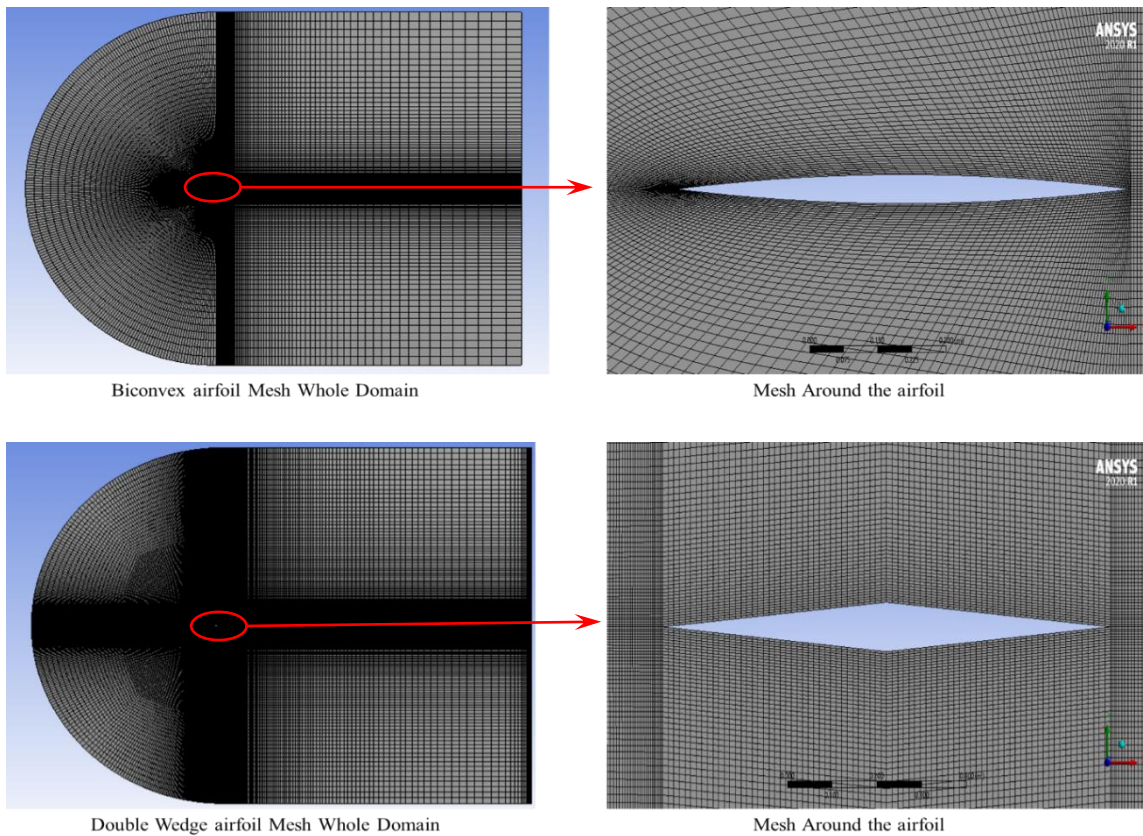


Figure 3. Mesh of the airfoils

2.8 Mesh Independence

A Mesh independency test was carried out using a series of simulations for both airfoils separately. By dividing circular and rectangular sections of the domain with different edge sizing, a different number of meshes were developed. These simulations were carried out for Mach 1.4 and 5° angle of attack for both airfoils. Figure 5 and Figure 6 shows how the lift coefficient varies with the number of mesh elements for Double-Wedge and Biconvex airfoils, respectively. As can be seen in the figures, meshes of more than 109438 elements (for Double-Wedge airfoil) and 40000 elements (for biconvex airfoil) able to generate precise results with minimal deviation. Consequently, for further simulation, the mesh with element numbers 109438 and 40000 was chosen for Double-Wedge and biconvex airfoil, respectively. For biconvex airfoil, skewness is limited to 1.3e-10 to 0.21, orthogonality is 0.11-0.9 and aspect ratio is 0.1, whereas for Double-Wedge airfoil, these are 1.31e-10 to 0.2, 0.8-0.9, and 1 respectively.

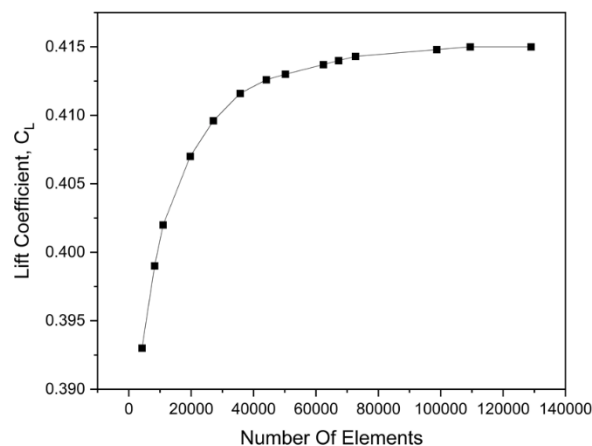


Figure 4. Variation of lift coefficient with number of elements double-wedge airfoil

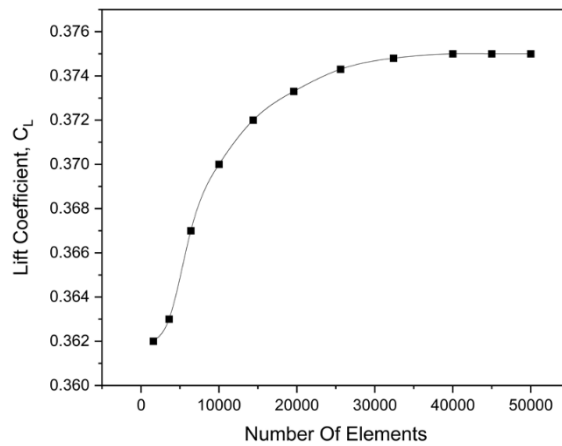


Figure 5. Variation of lift coefficient with number of elements biconvex airfoil

3.0 RESULT AND DISCUSSION

A 5% thick biconvex and a 5° half wedge angle Double-Wedge airfoil with a 1-meter chord length were modeled in supersonic flow. Around the airfoils, a C-type domain was created, and a structured quad mesh was developed. Due to the great compressibility of supersonic flow, a density-based solver was employed. Numerical solutions were found for the Navier-Stokes, Compressible Continuity, and energy equations. The Angle of Attack (α) ranges for both airfoils varied from 0° to 20° during a series of simulations for five different Mach numbers (1.4, 2.0, 2.4, 3.0, and 3.4). The distribution of pressure across the surface of the airfoils was numerically evaluated for each Mach number, Angle of Attack (α), Lift Coefficient (C_L), and Drag Coefficient (C_D). A RANS-based solver is used for solving the turbulence model.

The changes in lift coefficient (C_L) with angle of attack (AOA) (α) at Mach number 1.86 are compared to the results of Beastall D et al. [20]. Figure 7 compares the numerical results obtained in this study for a Double-Wedge airfoil with experimental results, linear theory, and shock-expansion theory. At a lower angle of attack up to 4° , the lift curves for all methods are linear and agree well with numerical results. The lift coefficient decreases at an 8° AOA compared to other methods, and at higher angles of attack, the experimental results provide a good approximation to the numerical results. When the linear theory curve and numerical results are compared, it is clear that even though the linear theory is based on plate configuration, it performs better at lower degrees of attack. The deviation from numerical results can be seen at higher degrees of attack. The Shock-Expansion theory is the exact theory for determining the aerodynamic lift and drag of a pointed airfoil, in this case, a Double-Wedge airfoil. When the numerical results and the Shock-Expansions theory results are compared in Figure 7, the curves almost coincide, confirming the validity of the numerical results found in this study. So, the results found numerically in the present work agree with the results of Beastall D et al. [31].

Figure 8 compares the numerical results for a biconvex airfoil obtained in this study to experimental and linear theory results. The numerical results are not compared because the Shock-Expansion theory only applies to pointed airfoils. When comparing experimental results to linear theory results, it can be seen in Figure 8 that the results obtained from linear theory are in very good agreement with the experimental results, and when comparing these two results to numerical results, it can be seen that the deviation from numerical results is comparatively very small at lower degrees of angle of attack. A slight deviation can be observed at higher degrees of attack, but the overall numerical result found is in good agreement with Beastall's results.

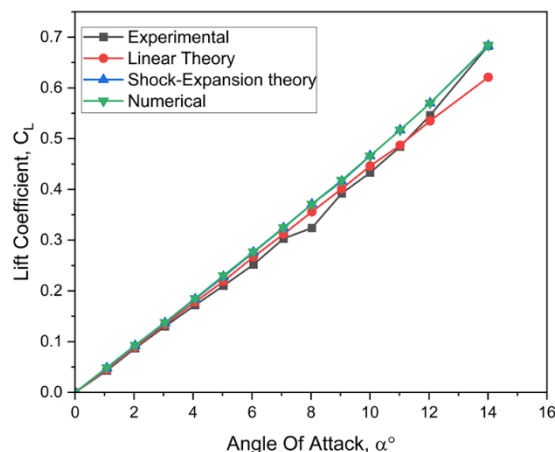


Figure 6. Comparison between the change in the coefficient of lift, C_L against the angle of attack, α with the result of Beastall D et al. [20] at Mach 1.86, Double-Wedge airfoil.

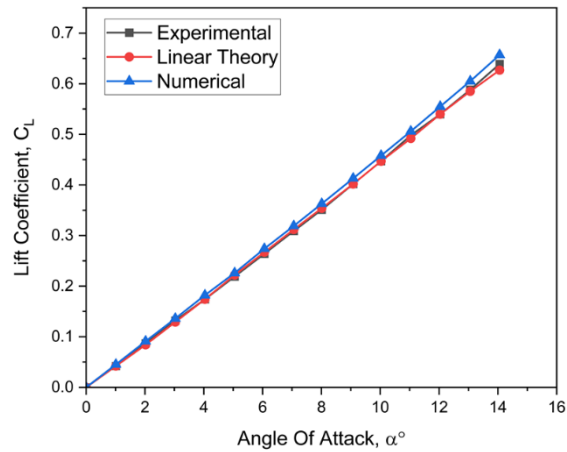


Figure 7. Comparison between the variation of C_L versus α with the result of Beastall D et al. [21] at Mach 1.86, Biconvex Airfoil.

3.1 Mach Number and Pressure Contours

The Mach number, pressure contours, and other results, namely the lift and drag coefficients and pressure coefficient distribution are extracted from the CFD post.

Mach number contours for fixed Mach, $M=1.4$, is shown in Figure 9, for both Biconvex and Double-Wedge airfoils for the angle of attack ranging, $\alpha = 2^\circ, 5^\circ, 10^\circ, 15^\circ, 20^\circ$. It is observed that an attached oblique shock wave is formed at the leading edge of both airfoils for $\alpha = 2^\circ$ and 5° ; after that expansion, a wave is created over the whole surface of the biconvex airfoil, but for Double-Wedge airfoil expansion wave is created at half chord location ($0.5C$) at $\alpha = 2^\circ$, for both the upper and lower surfaces and only at the upper surface at $\alpha = 5^\circ$. The downstream Mach number decreases after the attached oblique shock at the leading edge and increases after the expansion wave, and at the trailing edge, another oblique shock is formed, and the downstream Mach number again decreases to the free-stream value.

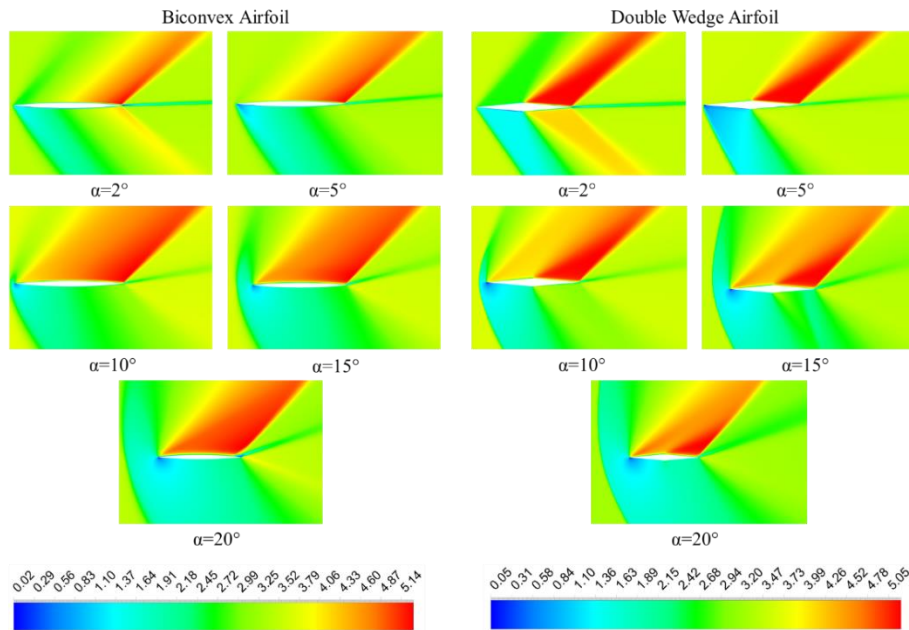


Figure 8. Mach number Contour of Mach 1.4 at Different Angle of Attack (α)

At $\alpha=10^\circ$, it can be observed that the attached oblique shock started to become a detached shock, and at $\alpha=15^\circ$ and $\alpha=20^\circ$, this detached shock formed a significant stern shock ahead of the leading edge. Bow shock formation reduces the Mach number to a minimum value of 0.02 for biconvex airfoil and 0.05 for Double-Wedge airfoil, respectively. Due to the formation of this bow shock, a discontinuity is created in the fluid flow domain, which reduces the velocity and pressure field. The maximum value of Mach number 5.14 for biconvex airfoil and 5.05 for Double-Wedge airfoil is observed at $\alpha=20^\circ$ at the upper surface of the airfoils.

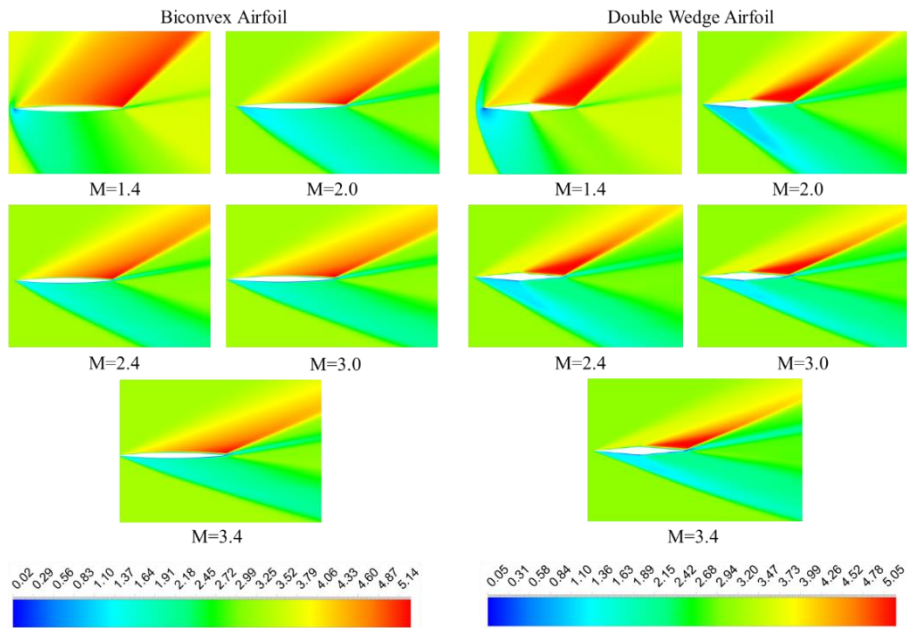


Figure 9. Mach number Contour at $\alpha=10^\circ$ for different Mach number

Figure 10 shows the Mach number contours for the angle of attack $\alpha = 10^\circ$ for different free-stream Mach numbers ranging from 1.4 to 3.4. It can be observed from the above figure that the detached shock formed at $M=1.4$ is becoming attached at the leading edge at Mach 2.0, and further increasing the Mach number decreases the shock angle, which indicates that the oblique shock is getting more attached to the airfoil surface for both the airfoils and the flow is getting towards the hypersonic regime, and the aerodynamic heating is taking place on the surface of the airfoils. For $M= 2.0, 2.4, 3.0, 3.4$, the downstream flow velocity is beginning to accelerate before the biconvex airfoil's half-chord length and after the Double-Wedge airfoil's half-chord length. The maximum value of the Mach number is 4.52 for the biconvex airfoil and 4.43 for the Double-Wedge airfoil is found on the upper surface at the trailing edge for both airfoils. The minimum Mach number value is equal to 0.27 for the biconvex airfoil and 0.32 for the Double-Wedge airfoil on the lower surface at the leading edge for both airfoils. Similar types of observations are found by observing the Mach number contours for the angle of attack $\alpha = 15^\circ$ for different Mach numbers, as shown in Figure 11. The maximum value of the Mach number is ($M=4.72$, for both airfoils) on the upper surface at the trailing edge for both airfoils. The minimum value of the Mach number is ($M=0.08$ for the biconvex airfoil and $M=.15$ for the Double-Wedge airfoil) on the lower surface at the leading edge for both airfoils.

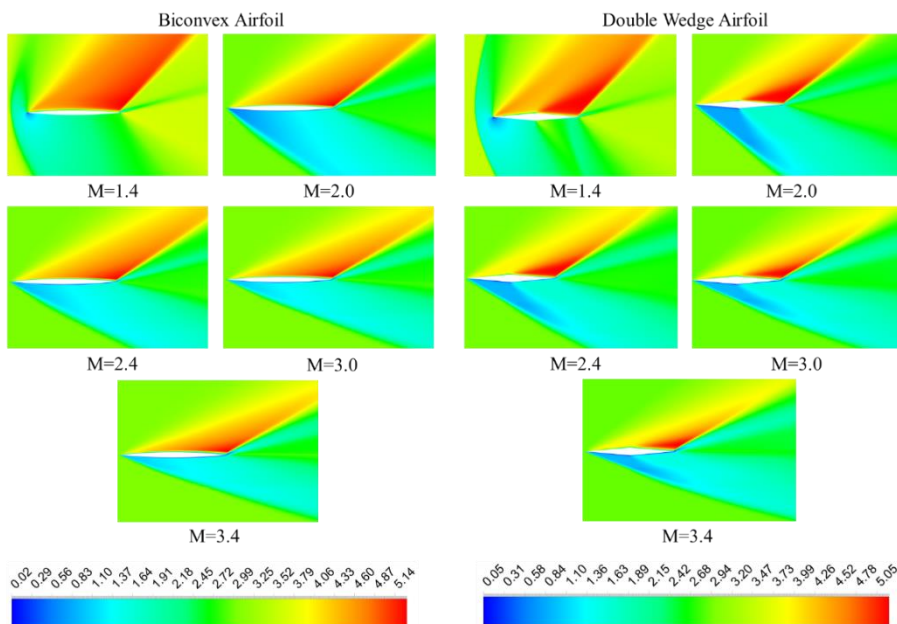


Figure 10. Mach number Contour at $\alpha=15^\circ$ for different free stream Mach number

The Mach Number contours for angles of attack, $\alpha=20^\circ$, are shown in Figure 12 for various Mach numbers. The figure shows that at $M=1.4$, the detached shock has transformed into a very powerful bow shock in front of the airfoils,

significantly increasing the drag and decreasing the lift. This powerful bow shock will start to attach as the Mach number rises and will fully attach after $M=2.0$. On the upper surface at the trailing edge of both airfoils, the maximum Mach number is ($M=5.14$ for a biconvex airfoil and $M=5.05$ for a double-wedge airfoil). On the lower surface at the leading edge of both airfoils, the minimum Mach number is $M=0.02$ for a biconvex airfoil and $M=.05$ for a double-wedge airfoil.

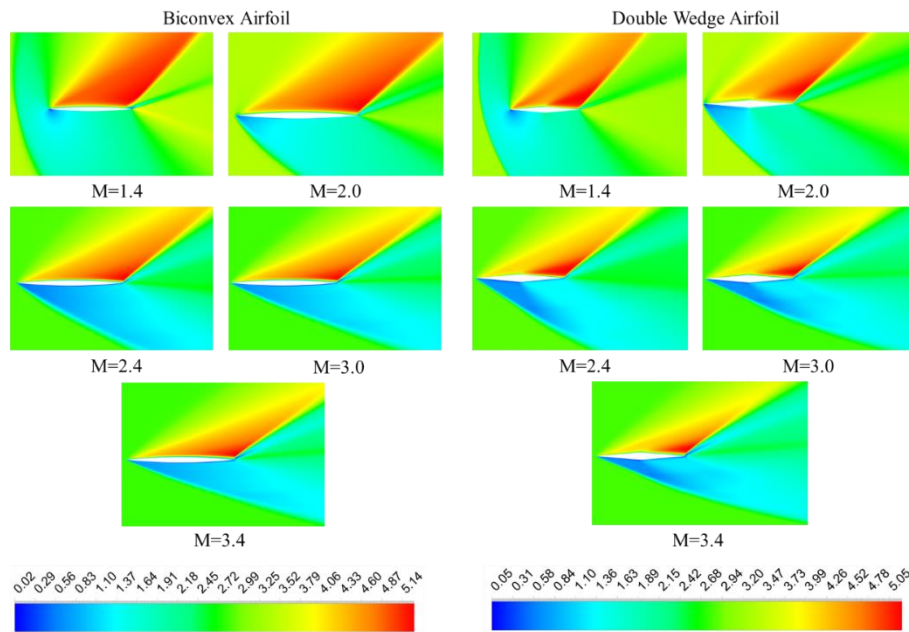


Figure 11. Mach number contours at $\alpha=20^\circ$ for different Mach numbers

Pressure contours for fixed Mach, $M=1.4$ is shown in Figure 13 for both Biconvex and Double-Wedge airfoils for Angle of Attack ranging, $\alpha = 2^\circ, 5^\circ, 10^\circ, 15^\circ, 20^\circ$. It is observed from the figure that the lower surface of the airfoils has a higher pressure region, and the upper surface has a lower pressure region, and pressure increases than the free stream value after the oblique shock wave and decreases after the expansion wave. At $\alpha = 2^\circ$, the maximum pressure occurs after the oblique shock at the leading edge at the lower surface of the airfoils. Still, the Double-Wedge airfoil has a wider area of higher pressure than the biconvex airfoil. Still, at $\alpha = 5^\circ$, a biconvex airfoil creates a higher value of pressure than the other airfoil, which is because for the biconvex airfoil, there is still an oblique shock created at the leading edge. On the contrary, there creates a weak Mach wave, and across the Mach wave, downstream pressure is lesser than the downstream pressure of an oblique shock for Double-Wedge airfoil as the half wedge angle and the Angle of Attack are the same. Further increasing the Angle of Attack (from $\alpha = 10^\circ$ to $\alpha = 20^\circ$), The Double-Wedge airfoil generates a wider area with a higher-pressure region than the other airfoil.

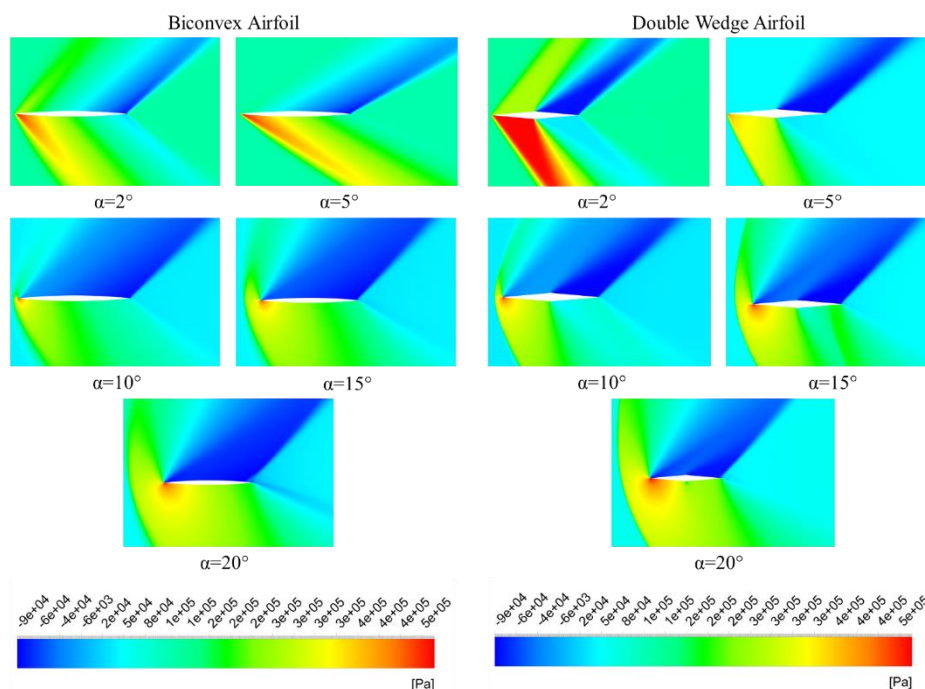


Figure 12. Pressure contour of Mach 1.4 at different angle of attack (α)

Figure 14-16 shows the Pressure contours for Angle of Attack, $\alpha = 10^\circ$, $\alpha = 15^\circ$, $\alpha = 20^\circ$, for different Mach Numbers, respectively. It can be observed from the figures that they show similar types of characteristics; for example, at $\alpha = 10^\circ$, the maximum pressure occurs downstream of the oblique shock created at the lower surface of the airfoils. Increasing the Mach number increases the maximum pressure value, and the highest is at $M=3.4$. The highest of the highest between these three Angle of Attack, shown in Figures 14,15,16, occurs at $\alpha = 20^\circ$, and the values are 498783 pascals and 483517 pascals for biconvex and Double-Wedge airfoil, respectively. So, the biconvex airfoil generates a higher value of maximum pressure than the Double-Wedge airfoil.

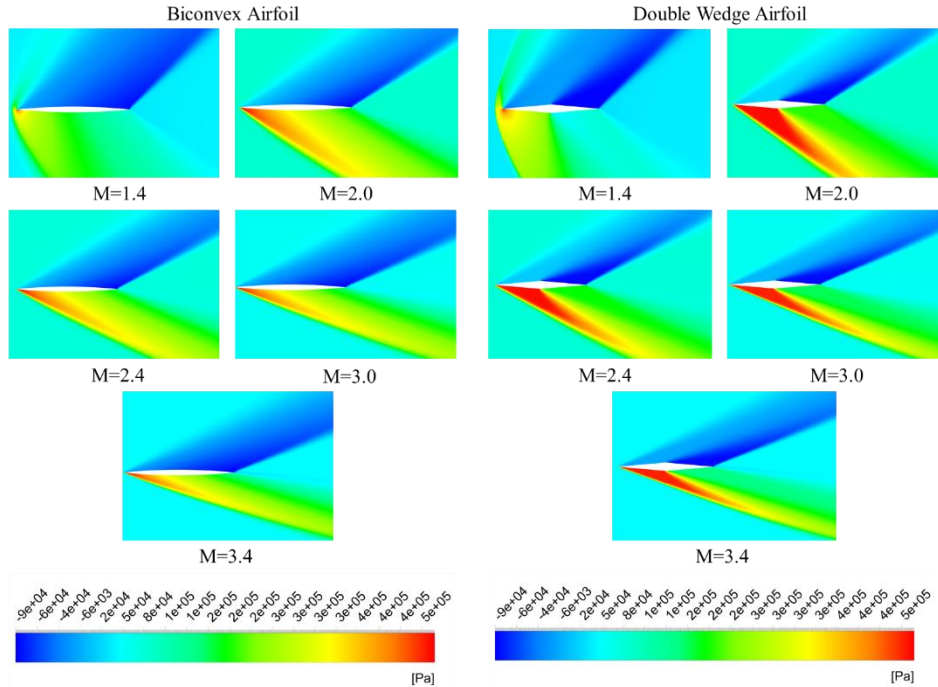


Figure 13. Pressure Contour at $\alpha=10^\circ$ for different Mach number

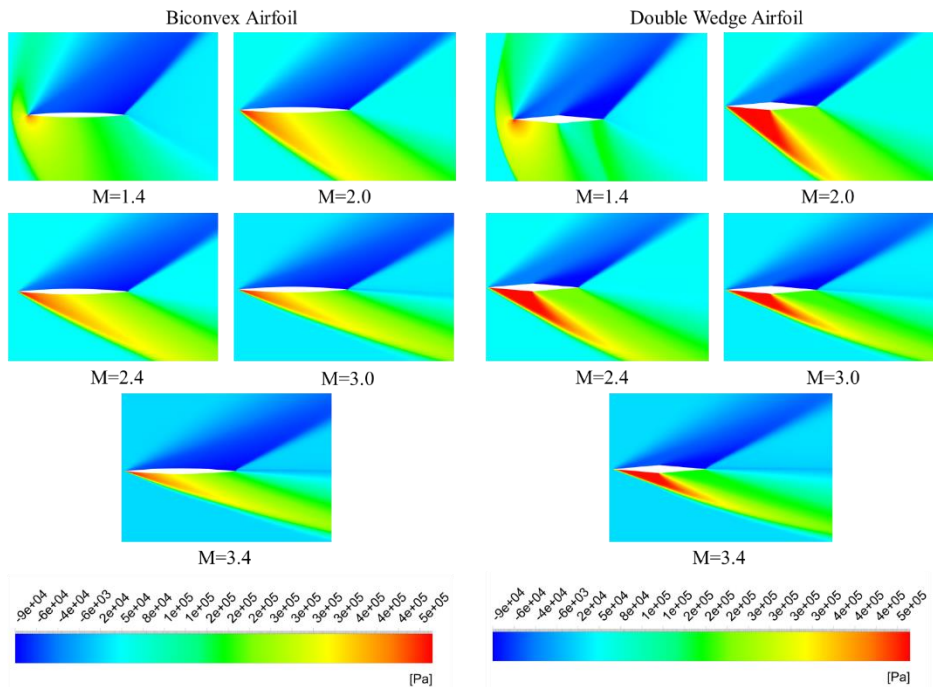


Figure 14. Pressure Contour at $\alpha=15^\circ$ for different Mach number

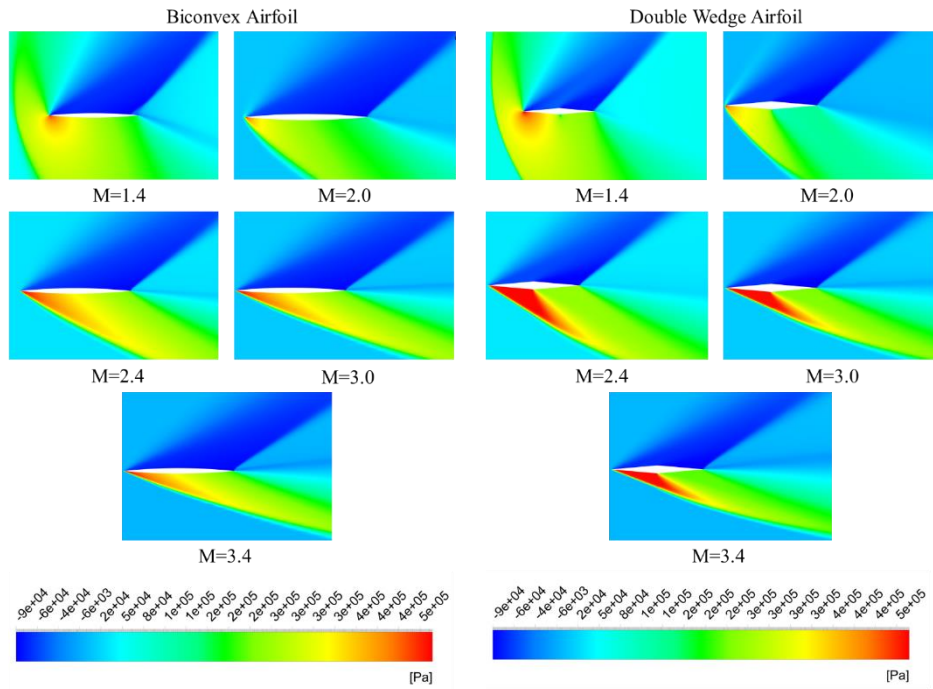


Figure 15. Pressure Contour at $\alpha=20^\circ$ for different Mach number

3.2 Effect of Lift and Drag Coefficient

The effects of lift coefficient and drag coefficient for different angles of attack for five different Mach values are depicted in Figure 17 and Figure 18, respectively. In supersonic flow over the thin airfoil, the lift coefficient follows the equation, $C_L = \frac{4\alpha}{\sqrt{M^2-1}}$. Based on the linearized theory, the lift coefficient increases for a fixed Mach number, increasing the angle of attack (α). As the denominator of the equation mentioned above suggests for a fixed angle of attack, increasing the Mach number decreases the lift coefficient; for example, for a 2° angle of attack, $C_L = 0.146$ at $M = 1.4$ and $C_L = 0.081$ at $M = 2.0$ for the biconvex airfoil, whereas, $C_L = 0.155$ at $M = 1.4$ and $C_L = 0.082$ at $M = 2.0$ for Double-Wedge airfoil. Therefore, for a fixed Mach number, increasing α will increase C_L , as observed in Figure 17; however, for all other Mach numbers, the C_L increase linearly with α for both the airfoils. For Mach 1.4, the lift curve is linear up to a 7° angle of attack for the biconvex airfoil, as shown in Figure 17(a), whereas up to $\alpha = 5^\circ$ for Double-Wedge airfoil as in Figure 17(b). A detached bow shock is created in front of the airfoil beyond the angle of attack 7° after that with increasing α , which reduces the lift. So, for the same parameters, a Double-Wedge airfoil generates almost 5% (at low Mach number) and more than 1% (at higher Mach number) more lift than a biconvex airfoil.

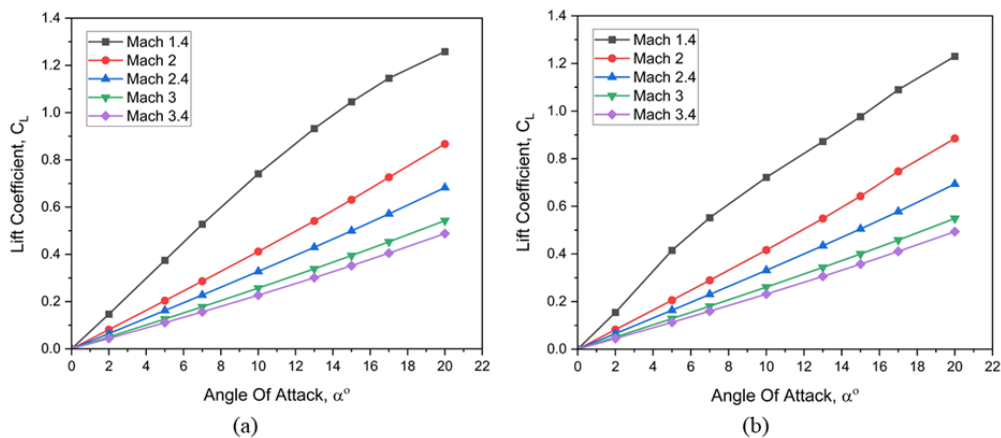


Figure 16. Lift coefficient versus angle of attack (α) at different Mach numbers (a) Biconvex airfoil and (b) Double-Wedge airfoil

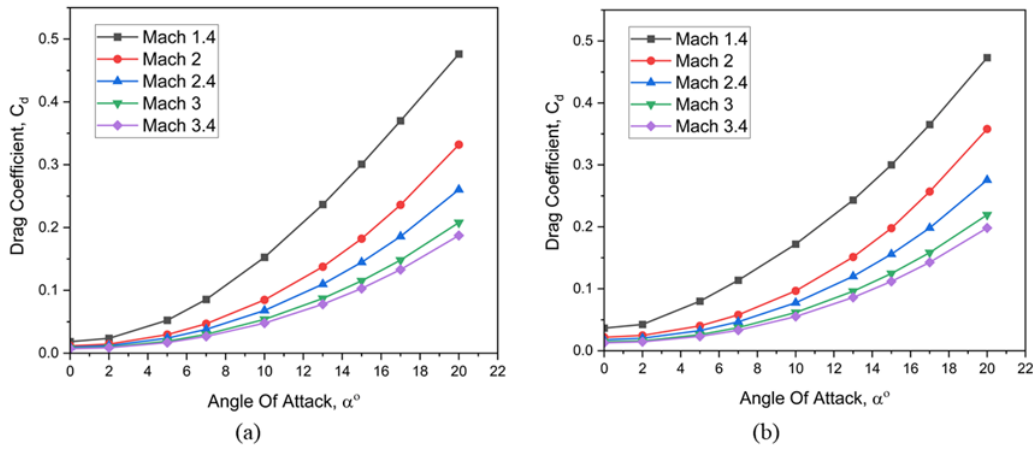


Figure 17. Drag coefficient plot against the angle of attack (α) at different Mach numbers (a) Biconvex airfoil and (b) Double-Wedge airfoil

Figure 18 illustrates how the drag coefficient increases with increasing the angle of attack (α) for a fixed Mach number and increases with increasing the Mach number for a fixed angle of attack (α). For instance, the drag coefficient with a biconvex airfoil at Mach 1.4 and 2.0 is found to be 0.024 and 0.014, respectively, for a given 2° angle of attack. At Mach numbers 1.4 and 2.0, the drag coefficients for a Double-Wedge airfoil are 0.043 and 0.025. The drag greatly increases shortly after $\alpha = 7^\circ$ for a biconvex airfoil, as seen in Figure 18(a), and $\alpha = 5^\circ$ for a Double-Wedge airfoil, as seen in Figure 18, due to the formation of a strong detached bow shock wave in front of the airfoils as previously noted.

3.3 Effect of Lift-to-Drag Ratio

The lift-to-drag ratio ($\frac{C_L}{C_d}$) compares the amount of lift produced by a wing or airfoil to its drag. The lift-to-drag ratio expresses the relationship between lift and drag by dividing the lift and drag coefficients. The $\frac{C_L}{C_d}$ ratio indicates the efficiency of an airfoil. Higher $\frac{C_L}{C_d}$ ratio aircraft are more efficient than lower $\frac{C_L}{C_d}$ ratio aircraft. The lift-to-drag ratio against the angle of attack for different Mach numbers is plotted and shown in Figure 11 for both airfoils. From Figure 19, it can be seen that the values of the lift-to-drag ratio ($\frac{C_L}{C_d}$) increase with angle of attack (α) up to a maximum value and then decrease to a minimum. According to Figure 20, the highest values of $\left(\frac{C_L}{C_d}\right)_{max}$ are determined to be 7.63, 7.18, 6.96, 6.77, and 6.66 for Mach 1.4, 2.0, 2.4, 3.0, and 3.4 at 3.46° , 3.72° , 3.89° , 3.99° , and 4.05° angle of attack, respectively. Figure 20 displays the numbers for a Double-Wedge airfoil. For Mach 1.4, 2.0, 2.4, 3.0, and 3.4, respectively, maximum $\frac{C_L}{C_d}$ is at an angle of attack of 4.47° , 5.09° , 5.38° , 5.55° , and 5.75° , and the corresponding maximum values of $\frac{C_L}{C_d}$ are 5.19, 5.16, 5.07, 4.97, and 4.92. These statistics show that the value of $\left(\frac{C_L}{C_d}\right)_{max}$ decreases as the Mach number increases because the lift coefficient increases and the drag coefficient decreases. It is also clear from Figures 19 and 20 that biconvex airfoils $\frac{C_L}{C_D}$ are larger than Double-Wedge airfoils because, for a given set of parameters, biconvex airfoils produce less drag as the angle of attack increases. In contrast, Double-Wedge airfoils produce more drag as the angle of attack increases.

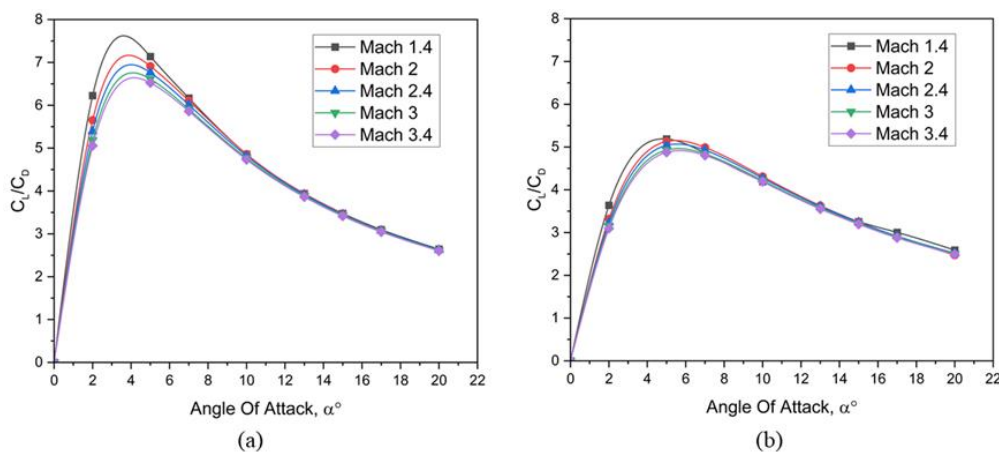


Figure 18. Changes of lift-to-drag ratio versus angle of attack (α) at different Mach numbers (a) Biconvex airfoil and (b) Double-Wedge airfoil

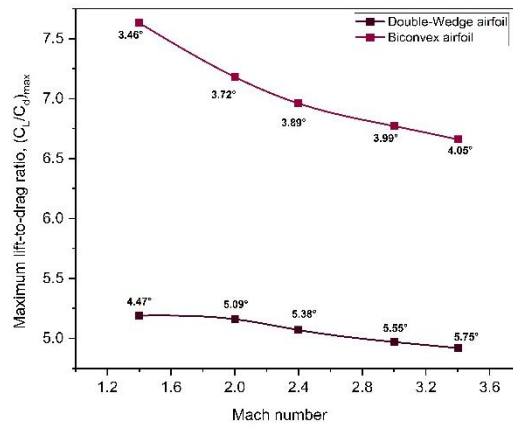
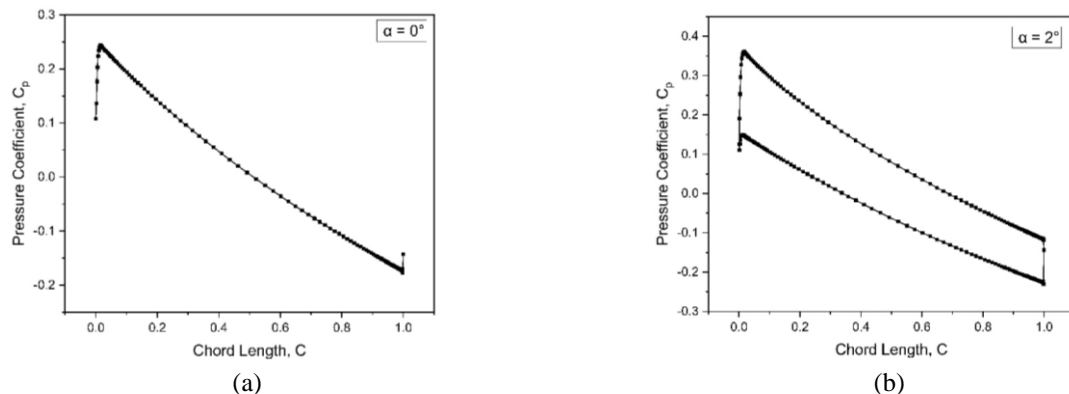


Figure 19. Maximum lift-to-drag ratio versus Mach number

3.4 Effect of Pressure Coefficient (C_p)

The coefficient of pressure (C_p) is a non-dimensional quantity that defines the relative pressures in a flow field. The pressure at all places surrounding an airfoil makes up this pressure distribution. Graphs of these distributions are typically drawn with negative numbers higher on the graph, as the C_p for the airfoil's upper surface is usually lower than zero, hence the top line on the graph. Figure 21 depicts the pressure coefficient (C_p) distribution along a biconvex airfoil at Mach 1.4 for different angles of attack (α). This Mach number was chosen because, as shown in sections 3.1 and 3.2, the lift and lift-to-drag curves are higher at this Mach number than at other Mach numbers. The distribution of C_p over the upper and lower surface is similar and symmetric at $\alpha=0^\circ$, as shown in Figure 13(a), which is why at $\alpha=0^\circ$, a biconvex airfoil, which is a symmetric airfoil, does not produce any lift. By increasing the angle of attack, the surface pressure distribution is no longer symmetric, and maximum C_p is obtained at the lower surface of the airfoil. As shown in Figure 21, with increasing the angle of attack, the point of maximum C_p also increases, and the area of the graph indicates the rise of the lift coefficient. At $\alpha=20^\circ$, the maximum coefficient of pressure is 1.7. It can also be seen from Figure 21(e-f) that, at $\alpha=15^\circ$ and $\alpha=20^\circ$, the pressure distribution is not uniform at the upper surface towards the trailing edge. The reason is that the oblique shock wave is advancing towards the leading edge from the trailing edge, and the flow is separating from the surface and reversing downstream of the oblique shock, as shown in Figure 9. Figure 22 shows the pressure coefficient (C_p) distribution along the Double-Wedge airfoil for different angles of attack (α) at Mach 1.4.

By observing Figure 22(a-f) and comparing it with Figure 21 for a Double-Wedge airfoil, the area and the trend of the curve are similar for both airfoils. In addition, it can be seen from the graphs, at $\alpha=15^\circ$ and $\alpha=20^\circ$, Figure 14(e-f), the pressure distribution is uniform at the upper surface towards the trailing edge. The Maximum value of C_p occurs at $\alpha=20^\circ$, and the value is $(C_p)_{max} = 1.4$ for Double-Wedge airfoil. Hence, comparing this maximum C_p to that of a biconvex airfoil, the biconvex generates a 17.6% higher value of the maximum C_p . An expansion wave is created whenever supersonic flow is turned away from the direction of flow. The flow properties change across the expansion wave: pressure decrease and flow velocity increase. On the other hand, an oblique shock wave is created whenever the flow turns itself in the direction of flow. The flow properties change across the oblique shock wave; namely, pressure increases and flow velocity decreases [32]. For this reason, the pressure coefficient increases after the leading edge of the biconvex airfoil, where an oblique shock is created, and it gradually decreases till the trailing edge as after the leading edge before the trailing edge expansion wave is created over the airfoil surface, shown in Figure 21. The maximum thickness for a Double-Wedge airfoil is $0.5C$, where the downstream surface makes a negative slope. For this reason, the flow is turned away, and an expansion wave is created; for this reason, after $0.5C$, the value of C_p decreases to a minimum for all angles of attack, as shown in Figure 22.

Figure 20. At Mach 1.4, the pressure coefficient (C_p) distribution over the surface of the Biconvex airfoil is shown for (a) $\alpha=0^\circ$, (b) $\alpha=2^\circ$,

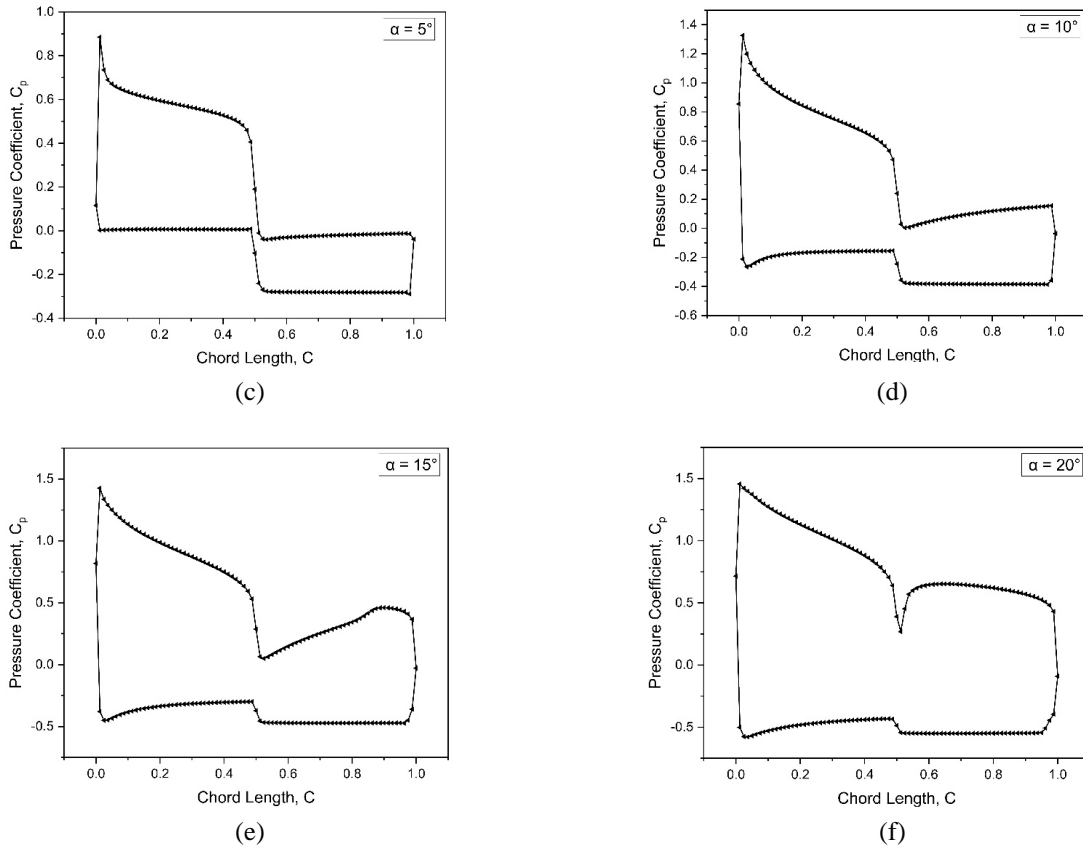


Figure 21. (cont.), (c) $\alpha=5^\circ$, (d) $\alpha=10^\circ$, (e) $\alpha=15^\circ$, (f) $\alpha=20^\circ$

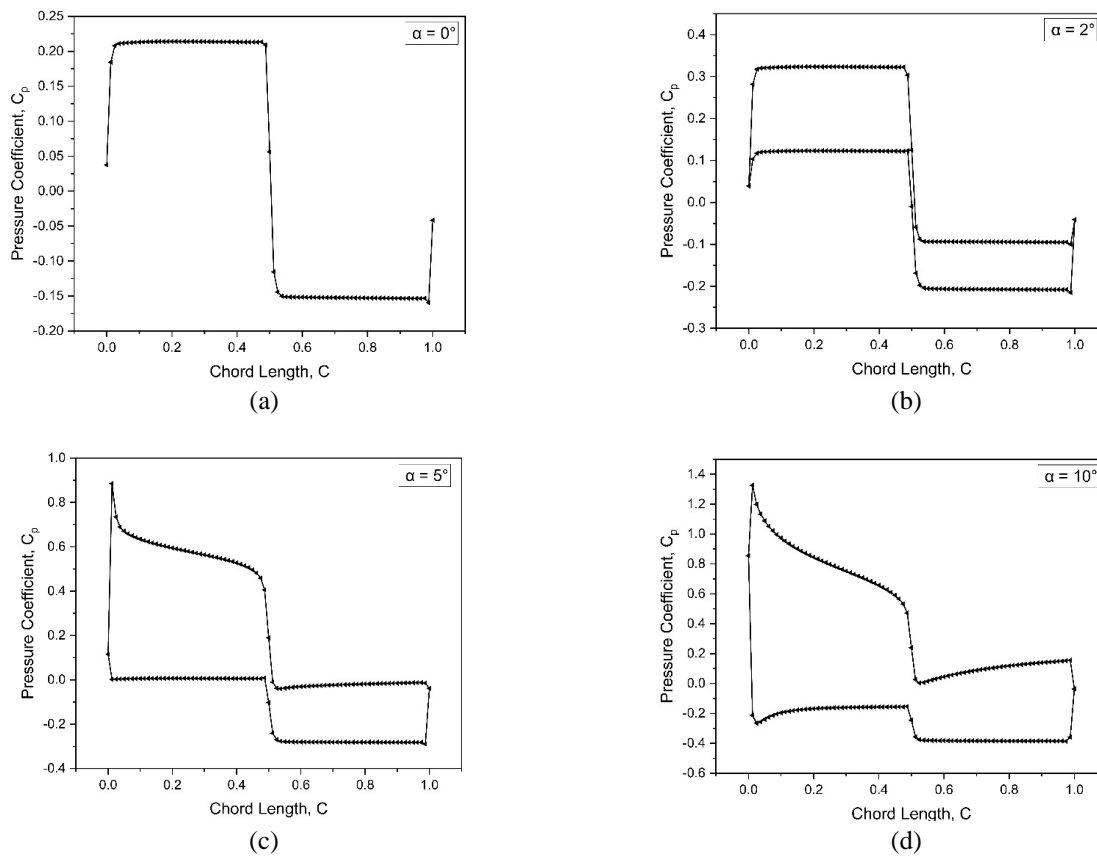
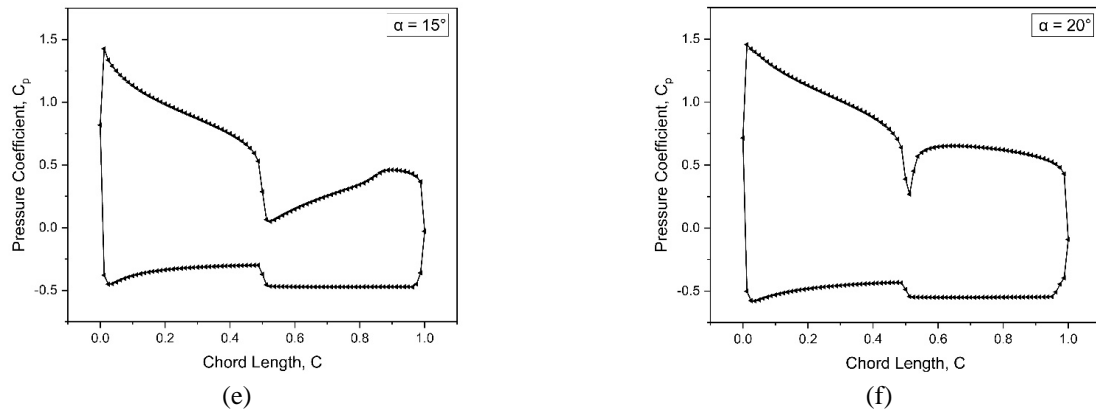


Figure 22. At Mach 1.4, the pressure coefficient (C_p) distribution over the surface of the Double-Wedge airfoil is shown for (a) 0° , (b) 2° , (c) 5° , (d) 10° ,

Figure 23. (cont.), (e) = 15° , and (f) = 20°

From the numerical analysis, it can be observed that the biconvex airfoil has a higher value of $(C_p)_{max}$ than the Double-Wedge airfoil for the same parameters. Both biconvex and Double-Wedge airfoil generate more lift at Mach 1.4 with the increase in the angle of attack (α) than other Mach numbers. Still, a Double-Wedge airfoil generates comparatively more lift than a biconvex airfoil for the same parameters. On the other hand, both the airfoils generate drag with increasing angle of attack (α), but the biconvex airfoil generates less drag than the Double-Wedge airfoil. For this reason, the biconvex airfoil has a higher lift-to-drag ratio. So, a biconvex airfoil gives a better aerodynamic performance for the same parameters than a Double-Wedge airfoil.

5.0 CONCLUSIONS

In the current investigation, numerical analysis was used to investigate the aerodynamic qualities of biconvex and Double-Wedge airfoils. A series of simulations were performed using ANSYS software. RANS-based solver is used, and the SST $k-\omega$ model is used for viscous modeling. The major findings of this research are:

- At Mach 1.4, a detached bow shock wave is formed in front of both airfoils at 10° , 15° , and 20° angles of attack.
- At 2.0-3.4 Mach numbers, the detached shock wave created in front of both airfoils at Mach 1.4 becomes attached to the surface for all angles of attack.
- For the same angle of attack and Mach number, the biconvex airfoil has a maximum C_p of 1.7, but the double-wedge airfoil has a maximum C_p of 1.4. As a result, a biconvex airfoil has a higher maximum pressure distribution than a double-wedge airfoil.
- At Mach 1.4, biconvex airfoils have a maximum lift-to-drag ratio of 7.63, compared to 5.19 for double-wedge airfoils. As a result, a biconvex airfoil has a higher lift-to-drag ratio than a double-wedge airfoil. Biconvex airfoils outperform Double-Wedge airfoils in terms of overall aerodynamic performance based on the greatest lift-to-drag ratio.

6.0 ACKNOWLEDGEMENT

The authors gratefully acknowledge the computation support provided by the Department of Mechanical Engineering, Khulna University of Engineering and Technology.

7.0 REFERENCES

- [1] T.J. Tharkude and Z. Li "Simulation Study of Supersonic Natural Laminar Flow on Wing with Biconvex Airfoil," *International Journal of Engineering Research & Technology (IJERT)*, vol. 7, no. 3, 2018.
- [2] H. Noubel and V. Lago, "Correlation between waverider shock waves and aerodynamic forces in supersonic rarefied flow, experimental investigation in the wind tunnel MARHy," *Acta Astronautica*, vol. 199, pp. 86-102, 2022.
- [3] J. Siegler, J. Ren, L. Leifsson, S. Koziel, and A. Bekasiewicz, "Supersonic Airfoil Shape Optimization by Variable-fidelity Models and Manifold Mapping," *Procedia Computer Science*, vol. 80, pp. 1103-1113, 2016.
- [4] N. A. Vu and J. W. Lee, "Aerodynamic design optimization of helicopter rotor blades including airfoil shape for forward flight," *Aerospace Science and Technology*, vol. 42, pp. 106-117, 2015.
- [5] S. B. Bensiger and N. Prasanth, "Analysis of Bi-Convex Airfoil Using CFD Software at Supersonic and Hypersonic Speed," *Elixir International Journal*, vol. 53, pp. 11695-11698, 2012.
- [6] M. A. Hamid, A. T. Hasan, S. Alimuzzaman, S. Matsuo, and T. Setoguchi, "Compressible flow characteristics around a biconvex arc airfoil in a channel," *Propulsion and Power Research*, vol. 3, no. 1, pp. 29-40, 2014.
- [7] E. Kinaci, "Supersonic flow over a double circular airfoil," *Gas Dynamics Take Home Project 2013*, Department of Fluid Dynamics, University of Duisburg Essen, 2015.

- [8] H. Zhou, G. Wang, and Z. Liu, "Numerical analysis on flutter of Busemann-type supersonic biplane airfoil," *Journal of Fluids and Structures*, vol. 92, p. 102788, 2020.
- [9] L. Zhou, Y. Chen, and F. Chen, "Chaotic motions of a two-dimensional airfoil with cubic nonlinearity in supersonic flow," *Aerospace Science and Technology*, vol. 25, no. 1, pp. 138-144, 2013.
- [10] C. Tulita, S. Raghunathan, and E. Benard, "Drag reduction and buffeting alleviation in transonic periodic flow over biconvex aerofoils," in *24th International Congress of the Aeronautical Sciences*, pp. 1-13, 2004.
- [11] D.H Williams and A.H. Bell, "Tests on a 5-percent Biconvex Aerofoil in the Compressed Air Tunnel," *Aeronautical Research Council Reports and Memoranda*, 1950.
- [12] W. Jones and S. W. Skan, *Aerodynamic forces on biconvex aerofoils oscillating in a supersonic airstream*. ARC Report, No. 14336, 1950.
- [13] R. J. M. a. W. D. Beasley, "Low-Speed Aerodynamic Characteristics of a 17 -Percent Thick Airfoil Section Designed for General Aviation Applications," *National Technical Information Service, NASA TND 7428*,1973.
- [14] J. Olejniczak, G. Candler, M. Wright, H. Hornung, and I. Leyva, "High enthalpy double-wedge experiments," in *Advanced Measurement and Ground Testing Conference*, p. 2238, 1996.
- [15] S. Isaev, P. Baranov, I. Popov, A. Sudakov, and A. Usachov, "Improvement of aerodynamic characteristics of a thick airfoil with a vortex cell in sub- and transonic flow," *Acta Astronautica*, vol. 132, pp. 204-220, 2017.
- [16] M. A. Khan and K. Vigneshwar, "Aerodynamic Analysis of Supersonic Spikes for Drag Reduction," in *Global Perspectives on Robotics and Autonomous Systems: Development and Applications*: IGI Global, pp. 130-167, 2023.
- [17] F. Lozano, I. Rahbari, G. Lin, and G. Paniagua, "Stochastic boundary condition effects on supersonic leading edge blowing," *Computers & Fluids*, vol. 243, p. 105513, 2022.
- [18] L. Matak and K. K. Nikolić, "CFD analysis of F-16 wing airfoil aerodynamics in supersonic flow," in *The Science and Development of Transport—ZIRP 2021*: Springer, pp. 197-210, 2022.
- [19] M. Y. Ahmed, "Surrogates for the Aerodynamic Coefficients of Supersonic Airfoils," in *53rd AIAA Aerospace Sciences Meeting*, No. 0770, 2015.
- [20] K. O. Friedrichs and B. Pattison, *Supersonic flow and shock waves*. Interscience Publishers (1st Ed.), New York, 1948.
- [21] R. D. Zucker and O. Biblarz, *Fundamentals of gas dynamics*. John Wiley & Sons, New Jersey, 2019.
- [22] J. J. Bertin and R. M. Cummings, *Aerodynamics for engineers*. Cambridge University Press, 2021.
- [23] H. Huang, T. Sun, G. Zhang, L. Sun, L. Sung and Z. Zong, "Modeling and computation of turbulent slot jet impingement heat transfer using RANS method with special emphasis on the developed SST turbulence model," *International Journal of Heat and Mass Transfer*, vol. 126, pp. 589-602, 2018.
- [24] B. E. Launder, "First steps in modelling turbulence and its origins: a commentary on Reynolds on the dynamical theory of incompressible viscous fluids and the determination of the criterion," *Philosophical Transactions of The Royal Society A Mathematical Physical and Engineering Sciences*, vol. 373, no. 2039, p. 20140231, 2015.
- [25] S. P. Sarathi Pattnaik and NKS. Rajan, "Computation of viscous flow characteristics of a supersonic intake using eddy-viscosity turbulence models," *Journal of Aerospace Engineering*, vol. 237, no. 4, pp. 865-882, 2023.
- [26] Z. Liu, P. Wang, B. Zhao, and C. Yang, "Assessment of a novel k- ω turbulence model for transonic centrifugal impeller simulations," *Transactions of the Canadian Society for Mechanical Engineering*, vol. 46, no. 3, pp. 587-601, 2022.
- [27] F. R. Menter, "Two-equation eddy-viscosity turbulence models for engineering applications," *AIAA Journal*, vol. 32, no. 8, pp. 1598-1605, 1994.
- [28] F. Menter, "Zonal Two Equation k-w Turbulence Models for Aerodynamic Flows," in *23rd Fluid Dynamics, Plasmadynamics, and Lasers Conference*, pp. 1-21, 2012.
- [29] M. S. H. Dudul, M. S. Mahmud, M. A. A. Islam, "Low-Fidelity Aerodynamic Load Analysis of Helicopter Rotor in Hover," *Astronautics, and Aviation*, vol. 55, no. 2, pp. 159-167, 2023.
- [30] E. Hosseini, "CFD analysis of the aerodynamic characteristics of biconvex airfoil at compressible and high Mach numbers flow," *SN Applied Sciences*, vol. 1, no. 10, pp. 1-8, 2019.
- [31] D. Beastall and R. Pallant, "Wind-tunnel tests on two-dimensional supersonic aerofoils at $M= 1.86$ and $M= 2.48$," *Aeronautical Research Council Reports & Memoranda*, 1950.
- [32] J. D. Anderson Jr, *Fundamentals of Aerodynamics*. Tata McGraw-Hill Education, 2010.